Acta Scientific Applied Physics

Volume 2 Issue 4 April 2022

Research Article

Investigation of Al-doped ZnO Thin Films Based on Powders Prepared Via Chemical Precipitation Method in Polyols

Mariem Louhichi[1], Zied Ben Hamed[1]*, Chadlia El Manaa[1,4], Samir Romdhane[1,2], Shaimaa Ali[3] and Habib Bouchriha[1]

[1]Laboratoire Matériaux Avancés et Phénomènes Quantiques, Faculté des Sciences de Tunis, Université El Manar, Tunis, Tunisia

[2]Faculté des Sciences de Bizerte, Université de Carthage, Tunisia

[3]Center for Photonic and Smart Materials (CPSM), Zewail City of Science and Technology, Sheikh Zayed District, Giza, Egypt

[4]Department of Physics, Jazan University, Jazan, Jazan Saudi Arabia

***Corresponding Author:** Zied Ben Hamed, Laboratoire Matériaux Avancés et Phénomènes Quantiques, Faculté des Sciences de Tunis, Université El Manar, Tunis, Tunisia.

Received: February 28, 2022

Published: March 31, 2022

Abstract

Al-doped zinc oxide (ZnO: Al%) based on powders prepared via Polyol method is deposited on glass substrate by spin coating. Samples were annealed at 220°C, 295°C, and 370°C for 1 hour in ambient conditions. The effects of annealing and aluminum doping concentration (Al%) on the structural and optical properties of ZnO: Al% thin films are investigated by X-ray diffraction, AFM, and UV-Vis-IR spectroscopic techniques. The smallest crystallite size for ZnO: Al% is obtained with 0.6% doping owing to the formation of Al-O-Zn in the crystal lattice. The microstrain (ξ) decreases with the increasing T_A which confirms the improvement of the crystalline quality of thin films. The AFM data are used to illustrate the surface morphology variation of thin films at different T_A as well as Al% content. We also showed that the optical constants are considerably influenced by the Al% and T_A. Photoluminescence spectra of ZnO: Al% powders analyzed based on Franck-Condon progression.

Keywords: Al-doped ZnO Thin Films; Polyol Method; X-ray Diffraction; Transmission; AFM

Introduction

Zinc oxide belongs to the II-VI compound with excellent semiconducting and piezoelectric double properties. It has been a standout amongst the most encouraging materials in the light of its potential use in numerous applications accredited to its wide and direct bandgap (3.37 eV), excellent chemical and thermal stability, and specific electrical and optoelectronic property [1]. These applications are running from antireflection coatings, straightforward anodes in sun-powered cells [2], Dye-Sensitized Solar Cells (DSSCs) [3], sensors [4], varistors, spintronic, photodetectors, surface acoustic wave devices [5], to light-emitting diodes [6], to nanolasers [7]. Numerous techniques have beforehand been used to deposit ZnO films on various substrates. These include filtered vacuum arc [8], sol-gel process, spray pyrolysis technique, sputtering, electrodeposition, chemical vapor deposition, pulsed laser deposition, molecular beam epitaxy, electron beam evaporation, and chemical bath deposition.

When zinc oxide nanoparticles doped with aluminum thin film becomes especially attractive as a transparent conductive oxide (TCO) in the light of its high conductivity, transmittance, thermal constancy, and non-toxicity [9]. Recently, different techniques are employed for the deposition of ZnO: Al% thin film with a dif-

ferent aluminum ratio. K. Mahmood., *et al*. [10] demonstrate the electrostatic spray deposition method for (ZnO: Al%) thin film at atmospheric pressure followed by annealing. They found that ZnO: Al% films have an arbitrary orientation with minimized hexagonal wurtzite structure with a sign of improvement in the electrical conductivity and optical properties upon annealing and Al doping. Employing a low-pressure chemical vapor deposition technique by W.Kim., *et al*. [11] indicated, however, a slight increase in the growth rates of ZnO: Al% films with the increase in the Al content. The resistivity was unequivocally subject to the carrier concentration and connected with the optical band gap and work function. All films displayed high optical transmittance in the visible range and high work function regardless of the Al content.

Then, A.C. Galca., *et al*. [12] prepared ZnO: Al% and ZnO: Lithium thin films by pulsed laser deposition technique and demonstrate the impact of the handling parameters on the optical and structural properties of doped ZnO thin films. The post-annealing treatment connected to ZnO: Al% thin films, strongly affected the optical properties, by bringing down the resistivity and red shifting the bandgap. V. Shelke., *et al*. [13] also use the spin coating technique to deposit thin films nanostructures of ZnO: Al%. The Electrical, optical and structural properties of these films showed that legitimate advancement of process parameters alongside Al percentage is required for enhancing the film quality in the view of minimizing roughness and rugosity [14].

In our previous work, we have studied the optical properties of ZnO: Al% powders fabricated based on the polyol method, which allows us to obtain ZnO nanoparticles with a narrower size distribution, a controlled morphology, and a high crystalline quality [15]. In the present study, we extend our work to investigate deeply the effect of different Al doping concentrations and annealing temperatures on the structural and optical properties of ZnO: Al% thin films deposited by a spin coating method. In particular, optical parameters such as the optical band gap, Urbach energy, refractive index, extinction coefficient, dielectric permittivity, Photoluminescence are reliant on the several microstructural properties of these compounds. Accordingly, the determination of effective structure constants of mixtures in terms of the microstrain, dislocation density, rugoses, and surface topography variation of thin films is useful. The way of annealing at ambient and low-temperature conditions is necessary for less energy consumption and is cost-effective for industrial applications.

Experiment details

Nanoparticles preparation

ZnO nanoparticles were prepared via the chemical precipitation method in polyols described elsewhere [16]. Chemical and materials such as zinc acetate dihydrate [$Zn(CH_3COO)\bullet 2H_2O$], aluminum hydroxide, sodium hydroxide (NaOH), and distilled water were purchased from Sigma- Aldrich. They were dissolved in 80 ml of diethylene glycol (DEG). The solution was heated at 189°C, therefore, kept at this temperature under continuous mechanical agitation. After 6 h of reaction, the mixture was stored at room temperature to prevent the escape of vapors into the atmosphere, the precipitate was centrifuged, washed several times with ethanol, and then dried in a vacuum at 50°C for 12 h to obtain the white powder.

ZnO: Al% thin film fabrication

15 mg of ZnO: Al% powders were successively dissolved in 1 mL of ethanol. Then, it was kept at room temperature for the aging process for 24 hours to obtain a better nanoparticle dispersion and to improve the solution homogeneity.

Glass substrates are precleaned with detergent followed by action, ethanol, and deionized water in BRANSON 200 ultrasonic cleaner for 30 min each. The solutions were deposited as a thin layer on glass substrates using spin-coating techniques at 600 rpm for 30 s than 300 rpm for another 30 s using a LAURELL WS-400BZ-6NPP/LITE, forming ZnO: Al% thin films. ZnO: Al% thin films are annealed at various temperatures of 220, 295, and 370°C for 1h at the ambient air conditions. X-ray diffractometer (XRD: Philips PW 3710) is used to elaborate the crystal structure of the ZnO: Al% films using Cu Kα radiation (λ = 1.541 Å). Measurements are performed in the geometry of coupled θ-2θ changed between 30° and 70°. Optical transmittance is measured by UV 3100S Shimadzu Spectrophotometer in the wavelength range of 300-1800 nm while a pulsed laser with an excitation wavelength of 325 nm is used for the photoluminescence (PL) measurements. Surface topography and AFM scanning image are captured using a commercial s-SNOM (NeaSNOM, NeaSpec GmbH).

Results and Discussion

Photoluminescence characterization

Figure 1 demonstrates the PL profile for ZnO:Al% (0.2, 0.6 and 5%) nanoparticles at room temperature. Because of ZnO doped, the PL emission spectra show broadband situated in the ultraviolet

and visible range. It has been reported [17] that the luminescence band because of metal transition components doped ZnO is credited to the impact of doping. Different emissions in the visible and ultraviolet range detected, however, the centers responsible for these emission bands and their related recombination mechanism kinetics are not comprehended and more explanation is needed. For this reason, we reproduce the photoluminescence emission spectra of the ZnO: Al% nanoparticles in the light of Franck-Condon progression [18] as clearly observed in figure 1. The investigation of the fluorescence range by regular spaced vibronic bands and regular full width at half maximum (FWHM) of the peaks demonstrates that the distinction in energy between progressive peak is around 0.18, 0.21, and 0.1 eV for different Al content of 0.2%, 0.6%, and 5% respectively. The four successive peaks were used to model the first two emission bands while the six successive peaks were applied to the last one. The reduction in the emission with the increase in the Al concentration is attributed to the presence of the nonradiative recombination where the energy of the longitudinal optical phonon $\hbar\omega_{LO}$ is the difference in energy between successive peaks. Jin., *et al*. attributed the violet emission at 420 nm (2.95 eV) to the transition between radiative imperfections level and the valence band. These radiative deformities are identified with the interface traps existing at the grain. According to Jeong., *et al*. The violet emission at 401 nm (3.09 eV) is a result of the Zn vacancies (V_{Zn}) while Fu., *et al.* found an ultraviolet emission situated at 392 nm (3.16 eV) in ZnO films deposited on the silicon substrate. They thought that this emission started from the electron transition from the conduction band to the valence band [18]. The reproduce results indicated peaks centered at 2.64, 2.82, 3, and 3.19 eV in the ZnO doped with 0. 2% Al (Figure 1 (a)). Increasing the Al content to 0.6%, peaks are located at 2.53, 2.75, 2.97, and 3.19 eV as indicated in figure 1b. Similarly, peaks focused at 2.67, 2.73, 2.81, 2.89, 3.17, and 3.4 are obtained for ZnO with a 5% doping concentration of Al. Noteworthy changes are recognized at range 360-430 nm which compares to the recombination of free excitons through the exciton-exciton collision process. The ultraviolet luminescence peak located at 388 nm (3.19 eV) in the samples with 0.2% and, 0.6% is red shifted to 391 nm (3.17 eV) under the effect of increasing the Al percent to 5%. This action increases the zinc interstitials (Zun_i) defects, which could also be accounting for the ultraviolet luminescence peak present at 3.4 eV. Similarly, the violet and blue luminescence peaks identified at 2.82 and 3 eV are red-shifted to 2.75 and 2.97 eV then to 2.81 eV and 2.89 eV upon increasing in the Al concentration from 0.2 to 0.6 and 5% respectively, this redshift attributed to aluminum interstitials defects close to the Zun_i defects. The joined impact of the optical transition to the excitonic state of ZnO and electronic transitions including precious crystal-field split is in charge of the energy shifted.

Figure 1: Photoluminescence Franck Condon analysis as a function as photon energy of (a) ZnO:Al 0.2%, (b) ZnO:Al 0.6%, (c) ZnO:Al 5% nanoparticles.

Structural characterization

XRD analysis

The XRD analysis examinations of nanoparticles powders demonstrated the hexagonal Wurtzite structure and had a most favored introduction along the (101) plane. Likewise, the TEM results exposed that the average particle size of the samples diminishes by increment Al percentage. Moreover, the energy dispersive spectroscopy had made known the substitution of Al into ZnO lattice. The X-ray diffraction patterns for ZnO: Al% films as-deposited and annealed at various temperatures (T_A = 220°C, 295°C, and 370°C) are shown in figure 2 (a-c) the diffraction peaks are easily indexed based on the hexagonal-rhombohedral structure of ZnO: Al% (R-3c) The crystals of ZnO: Al% thin films when subjected to X-ray inspection have displayed the rhombohedral polytypes occurring consistently in conjunction with their individual basic hexagonal (hexagonal phase, space group P63mc). Similar results are found elsewhere [16]. This hexagonal-rhombohedral phase change is unfurling while crystal development can be effortlessly comprehended as far as stacking faults occurring periodically other during development or because of creation and development of Shockley partials, either produced independently or grace of separation of unit edge dislocations [20]. The formation of a particular structure in a compound, known under the name of a basic or common type, under stabilized conditions of growth, and the variation in stacking sequence of these structures because of the change in growth conditions [21], composition, or temperature [22] provide a general understanding of the mechanism of the of polytypes in these compounds. The rule of the basic types on all the other ones even if their energy differences are very low for all cases remains problematic. The association of all data helps us to understand, analyze, and refine better the structure of films. The amount of $ZnAl_2O_4$ and other ZnAlO species seems to stay approximately independent of growing temperature T_A and Al%. From the spectra presented in figure 2, we calculated the more interplane spacing d_{hkl} of the families of the crystalline plane (hkl) using Bragg's law. The texture coefficient (TC), the augment in the best orientation is related to the rise of the number of grains along that plane. $TC_{(hkl)}$ values are found from X-ray information utilizing the next expression [23]:

$$TC_{(hkl)} = \frac{I(hkl)/I_0(hkl)}{N^{-1}\sum I(hkl)/I_0(hkl)} \qquad \textbf{(1)}$$

(a)

(b)

(c)

Figure 2: XRD patterns of ZnO:Al 0.2% (a), ZnO:Al 0.6% (b) and ZnO:Al 5% (c) thin films with different T_A.

Where N, I(hkl), and I_0(hkl) are the reflection number, the measured and standard intensities of (hkl) direction, respectively.

Table 1 shows an example of the values of different crystallography parameters (the values of all samples are not presented here). Here once more, the grain size (D) esteems are evaluated for all diffraction lines utilizing Debye-Scherrer expression [24]:

2θ (°)	DHL (Å)	I_{max}	I_0	I_{max}/I_0	TC
31.84	0.834	65	3	21.66	2.858
34.51	1.214	33.98	100	0.34	0.045
36.34	3.54	68.42	93	0.73	0.097

Table 1: Values of DHL and $TC_{(hkl)}$ of prepared thin film (ZnO: Al 5% annealed at 220°C).

$$D = \frac{k.\lambda}{\beta_{1/2}\cos\theta} \qquad (2)$$

Where k = 0.90, λ = 1.5406 Å, $\beta_{1/2}$ and θ are the Scherrer constant, the wavelength of CuK**α** radiation, the Full-width at half-maximum (FWHM) of considered peak and the Bragg angle, respectively. Likewise, the microstrain (ξ), which is an interesting structural parameter of ZnO: Al% thin films, is calculated using the following relation [25]:

$$\xi = \frac{\beta_{1/2}}{4\tan(\theta)} \qquad (3)$$

The dislocation density (δ) is evaluated utilizing the next expression [26]:

$$\delta = \frac{1}{D^2} \qquad (4)$$

The likelihood made of the TC is for a given orientation. It can be utilized to ascertain the averages of D and ξ and can consequently outperform the Williamson and Hall expression [26] utilizing:

Table 2 shows an example of grain size, microstrain, and dislocation density values (the values of all samples are not shown here).

We note that the parameter c decreases from 14.670 Å to 13.988 Å corresponding to the increase in the Al content from 0.2 to 5% at room temperature. The same parameter shows no monotonic behavior for others temperatures (see Table 3). This variation in the lattice parameter c could be due to a probable substitution of Zn^{2+} by Al ions [27]. This substitution process could be affected by temperature. As seen in figure 3, the parameter a for ZnO: Al 0.2% thin films annealed with different temperatures at RT, 220°C, 295°C, and 370°C were found to be 4.968 Å, 4.963 Å, 4.965 Å, and 4.924 Å, respectively. The slope of this growing dependence on the Al%. The various structural parameters for ZnO: Al% (0.2%, 0.6%, and 5%) thin films at different T_A are calculated and represented in table 4. Various parameters such as dislocation density, microstrain, and grain size depend on the annealing temperature. The increase in Al% causes a non-intense diffraction peak with a broad full width at half maximum (FWHM), signifying the decrease in crystallite size. This results from the worsening of the film crystallinity due to the stress formed by the difference in ion size between zinc and aluminum (R_{Zn}^{2+} = 0.074 nm and R_{Al}^{3+} = 0.054 nm). The smallest crystallite size is obtained at 0.6% doping with Al and this could be as a result of the formation of Al-O-Zn in the crystal lattice, which plays a significant role in hindering the crystal growth [28]. With increasing Al content, the smaller crystallites size may gain a tendency to aggregate [29]. Figure 3 depicts the behavior of lattice parameters as a function of T_A. The values of the parameters grow slightly as a function of the T_A.

	Film	a = b (Å)	c (Å)
ZnO:Al 0.2%	RT	4.924	14.271
	T_A = 220°C	4.963	14.257
	T_A = 295°C	4.965	13.921
	T_A = 370°C	4.968	14.670
ZnO:Al 0.6%	RT	4.957	13.995
	T_A = 220°C	5.022	14.767
	T_A = 295°C	4.995	14.542
	T_A = 370°C	4.967	14.539
ZnO:Al 5%	RT	4.956	13.988
	T_A = 220°C	5.006	14.276
	T_A = 295°C	5.029	14.276
	T_A = 370°C	5.015	15.290

Table 3: Lattice parameters of all ZnO: Al% thin films.

Figure 3: Variation in the lattice parameter (a=b) of ZnO:Al 0.2%, 0.6% and 5% thin films as a function of T_A.

	Film	D (nm)	ξ (x10^{-3})	δ (10^{15} lines/m^2)
ZnO:Al 0.2%	RT	19.72	6.34	2.57
	T_A = 220°C	21.17	6.02	2.23
	T_A = 295°C	22.04	5.61	2.05
	T_A = 370°C	23.40	5.34	1.82
ZnO:Al 0.6%	RT	12.72	9.92	6.18
	T_A = 220°C	15.10	9.00	4.38
	T_A = 295°C	16.96	7.27	3.47
	T_A = 370°C	17.37	7.22	3.31
ZnO:Al 5%	RT	25.41	5.65	1.54
	T_A = 220°C	26.49	4.74	1.42
	T_A = 295°C	32.47	3.93	0.95
	T_A = 370°C	33.21	3.83	0.91

Table 4: Grain sizes, microstrain, and dislocation density of ZnO: Al% thin films annealed at various temperatures (220°C, 295°C, and 370°C).

The evolution of the crystallite size of ZnO: Al% thin film as a function of T_A is reported in figure 4 (a), and indicates an increase in the grain size with the increase in the T_A owing to the increase in the atoms mobility and crystallite cross involving to form larger grains [30]. The variation in the microstrain and dislocation density with T_A is presented in figure 4 (b and c) respectively and indicates the reduction of both values as a function of T_A which confirms the improvement in the crystalline quality and the deduction in the lattice defects.

(a)

(b)

(c)

Figure 4: Variation in the crystallite size (D) (a), microstrain (ξ) (b), and the dislocation density (δ) (c) of ZnO: Al% thin films as a function of T_A.

The inclusion of Al in the ZnO lattice is known to have the characteristic absorption of the Al-O stretching mode. In summary, the hypothesis that there is at least some of the carbon, oxygen, and hydrogen co-exist as defect complexes in the ZnO thin films. The heat treatment of the samples changes their lattice parameters. In other words, the annealing process causes a change of oxygen composition and oxygen defects such as oxygen vacancies (V_0) and oxygen interstitials (O_i). Also, this process creates a structural modification such as a change in the crystallite size, microstrain, and dislocation density. The variation of crystallite size is not shown as monotonous behavior, indicating that these evolution types are probably caused by an aggregation of many crystallites [31].

AFM microscopy

Atomic force microscope is employed to explore the surface topography of ZnO: Al% films annealed at 220°C and at different Al content of (0.2, 0.6, and 5%) As shown in figure 5. The variation in the surface topography image at different annealing temperatures T_A (220°C, 295°C, and 370°C) is shown in figure 6 for the sample containing 5% Al concentration. As indicated from the figures the film surfaces are consist of separate islands with dendrite shapes. Furthermore, the layer is constituted by small coalescent islands indicating reduced diffusion mobility of the ZnO: Al% molecules on the substrate. The different surface morphologies are evolved relying on T_A and Al%. The AFM images indicate the increase in the grain size with the annealing treatment which accordingly increases the surface roughness (see Figure 6). As for this the ZnO: Al 5% thin films annealed at 370°C has a higher surface roughness [32].

Figure 5: AFM images of ZnO: Al% (0.2, 0.6, and 5%) thin films annealed at 220°C in the air for 1 h.

Figure 6: AFM images of ZnO: Al 5% thin films for different T_A (220°C, 295°C, and 370°C) in the air for 1 h.

The behavior of surface rugosity is the same as the extracted grain size values from XRD. In contrast, the surfaces of ZnO: Al 5% thin films annealed at 220°C in the air become much smoother and more uniform than other samples with the same Al% content. Thus, the better structural quality smoothly, and uniformity of ZnO: Al 5% thin films are obtained when annealed at 220°C. This is confirmed by the root mean square (RMS) surface roughness. The RMS of ZnO: Al 5% thin films for different T_A (220°C, 295°C, and 370°C) in the air are about 13.87 nm, 25.66 nm, and 29.64 nm, respectively. This observation is in agreement with those found by X-ray diffraction analysis (see table 4). The tapping-mode topography AFM images of ZnO: Al% annealed at 220°C layers are shown in figure 5. Another important note is that the ZnO: Al 5% (annealed at 220°C) surface is rougher than that of the ZnO: Al 0.2% and ZnO: Al 0.6% (annealed at 220°C). The films became less homogeneous and showed severs aggregation, and we observed an increase in the extracted grain size values from XRD and a variation in the thickness of the device. The root means square (RMS) surface roughness of ZnO: Al% (0.2, 0.6 and 5%) thin films annealed at 220°C in the air are about 6.61 nm, 4.917 nm, and 13.87 nm, respectively.

Reflectance and transmittance spectra

The transmittance and reflectance measurements of ZnO: Al% thin films are scanned in the wavelength range of 300-1800 nm

using UV-Vis spectroscopy for all samples under consideration as shown in figure 7. The increase in the T_A had successfully enhanced the optical transmittance of the films. The average transmittance faintly varied along with the T_A, it increased from 79 to 85% for in the film containing 0.2% Al, from 65 to 84% in the case of doping with 0.6%, and from 84 to 88% as the T_A increased from 220°C to 370°C. However, it showed a very high increase compared with as-deposited film (increase about 8% for ZnO:Al 0.2%, 21% for ZnO:Al 0.6% and 33% for ZnO:Al 5%). This improvement is due to the better-formed crystallite and indicated that our annealing treatment was very efficient and improved the transmittance of ZnO: Al% films. From figure 8, all films have high transparency within the visible range with an average transmittance lying between 84% and 88% which means a good optical quality due to low scattering or absorption losses [33].

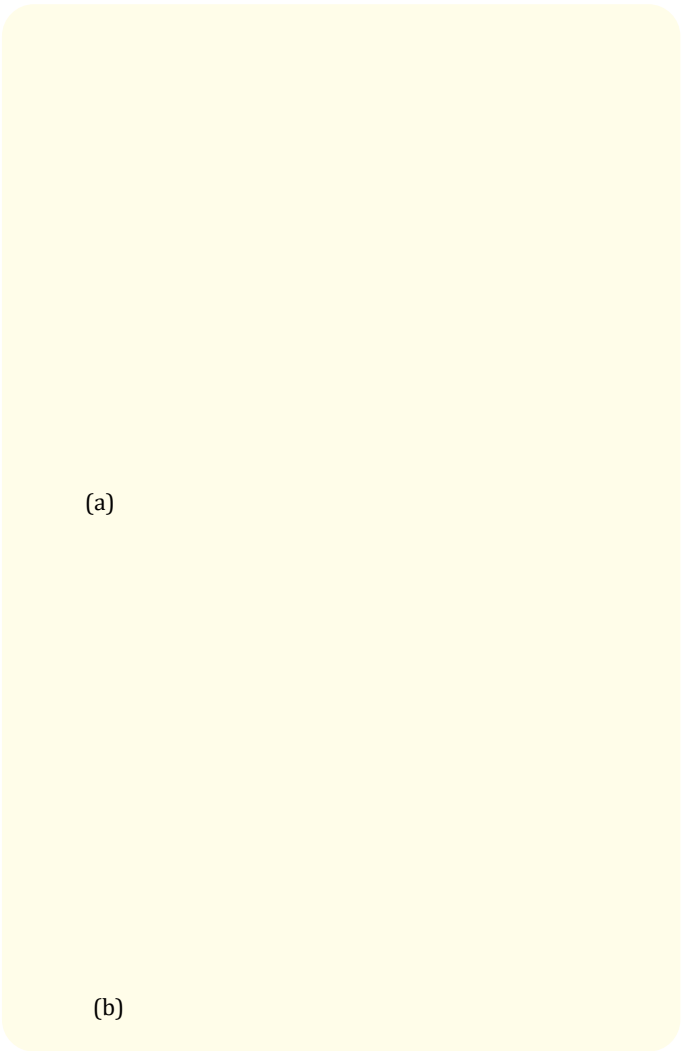

(a)

(b)

(c)

Figure 7: Transmission and reflection spectra of doped coated ZnO:Al 0.2% (a), ZnO:Al 0.6% (b) and ZnO:Al 5% (c) thin films as a function of T_A.

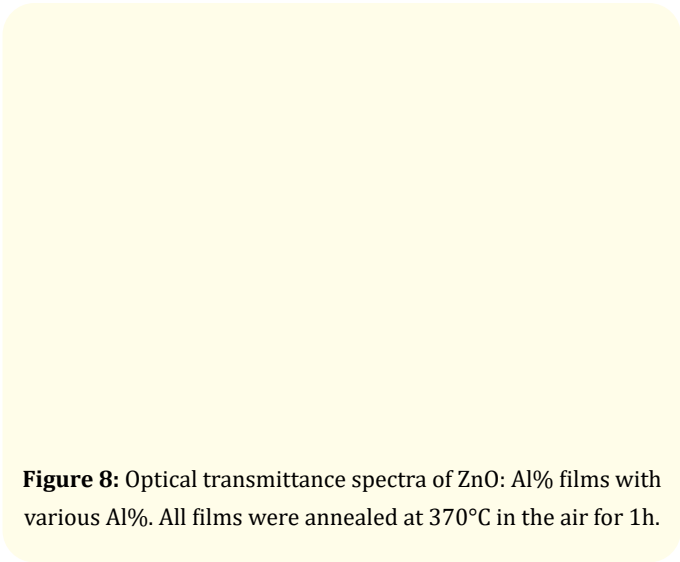

Figure 8: Optical transmittance spectra of ZnO: Al% films with various Al%. All films were annealed at 370°C in the air for 1h.

Bandgap energy and Urbach energy calculation

An analysis of the optical band-gap energy E_g of the thin films has been made using the optical absorption coefficient α determined by the next expression [34]:

$$\alpha = \frac{1}{d} Ln\left(\frac{(1-R)^2}{T}\right) \quad (7)$$

Figure 9 (a) illustrates an example of absorption coefficient evolution with the photon energy (ZnO: Al 5%) and figure 9 (b) presents an example of the plot ln(α) versus photon energy (ZnO: Al 5%).

As shown in Figure 9 (c), the optical band gap E_g esteems were concluded to agree with the formula [35]:

$$(\alpha h\nu)^2 = A(h\nu - E_g) \quad \textbf{(8)}$$

(a)

(b)

(c)

Figure 9: The plot of α (a), ln(α) (b) and (αhν)2 (c) versus photon energy of ZnO: Al 5% thin films.

Where A, E_g, and hν are constant characteristics of the semiconductor, the optical band gap energy, and the absorption coefficient, respectively. The optical band gap values are given in table 5 and show an increase from 3.50 eV to 3.63 eV with increasing doping percentage (Al) from 0.2% to 5%. This agrees with other workers [36], for increasing Al%. This effect is due to the Burstein-Moss effect, which implies an enhancement in the Fermi level in the conduction band of semiconductors due to increased carriers, leading to the widening of the optical band-gap [37].

	Film	α_0 (m^{-1})	E_g (eV)	E_u (meV)
ZnO:Al 0.2%	RT	0.213	3.50	215
	T_A = 220°C	0.480	3.48	226
	T_A = 295°C	0.110	3.43	208
	T_A = 370°C	0.176	3.39	213
ZnO:Al 0.6%	RT	0.073	3.53	205
	T_A = 220°C	0.060	3.42	203
	T_A = 295°C	0.158	3.45	214
	T_A = 370°C	0.133	3.39	210
ZnO:Al 5%	RT	0.071	3.63	206
	T_A = 220°C	0.027	3.54	195
	T_A = 295°C	0.007	3.50	183
	T_A = 370°C	0.004	3.43	179

Table 5: Optical gap, Urbach energy, and α_0 of ZnO: Al% thin films annealed at various temperatures.

The variation of the optical gap of ZnO: Al% thin films as a function of the T_A is reported in figure 10 which indicates a reduction in the optical gap values for all film samples as the T_A increased from 220-370°C. The cutback of the optical band gap with increasing T_A can be due to the enhanced crystallinity and decreased defects of the films. Similar results have been reported in the work of Jianguo., *et al.* [38] and Mudjat., *et al.* [39].

Figure 10: The plot of E_g versus T_A for ZnO: Al% thin films.

The growth of the crystallite size and the decrease of the microstrain are the main reason behind the performance of the optical properties. In the same context, the emergence of Al creates a permis state in the gap of ZnO thin films [40]. The apparent bandgap of a semiconductor is increased as the absorption edge is pressed to higher energies as a result of all states close to the conduction band being occupied. This is was observed for a degenerate electron diffusion such as that found in some degenerate semiconductors and is known as a Burstein–Moss shift [41].

In our layers, the Al species grown into and on the ZnO matrix caused this degenerate electron distribution and increase the gap energy for such T_A and Al% combination. The inclusion of an impurity into the semiconductor frequently results in the development of band tailing in the bandgap. The optical transitions between connected states in the valence band tail to unpopulated states of the conduction band edge prompt an exponential reliance of the absorption coefficient α on photon energy near the band edge. This implies the advancement of the Urbach energy could offer a thought regarding the immediate impact of Al% into ZnO lattice. The absorption spectra clarify a broadening tail for bringing down photon energies under the band edge, which can be depicted by [42]:

Where E_u, α, and α_0 are the Urbach energy corresponding to band tails width of the localized states in the bandgap, the experimentally deduced optical absorption profile and a constant, respectively. The values of E_u are calculated as the reciprocal gradient of the linear portion of the plot. As seen in table 5, the Urbach energy estimation for all thin-film samples with different T_A (220°C, 295°C, and 370°C) does not represent monotonous behavior. Urbach energy is expressing the stability of doping agents inside host structures which means in our case, the V_0 and O_i governed the optical response of our system.

Refractive index and extinction coefficient

The extinction coefficient (k) indicates the amount of attenuation when the electromagnetic wave propagates through the material. It is a frequency-dependent value that measures the energy loss of electromagnetic radiation. The reliance of the extinction coefficient on the wavelength in the range 350-800 nm of ZnO: Al% samples annealed at different temperatures are shown in figure 11. It is obvious that the values of k diminish in values of all wavelength (350-800nm), while it increases after annealing the samples (220, 295 and 370°C), this is attributable to the rise in absorption coefficient, where the extinction coefficient relies upon the absorption coefficient by the accompanying expression:

$$k = \frac{\alpha\lambda}{4\pi} \qquad \textbf{(11)}$$

(a)

(b)

(c)

Figure 11: Extinction coefficient k versus λ of ZnO:Al 0.2% (a), ZnO:Al 0.6% (b) and ZnO:Al 5% (c) thin films deposited at various T_A.

The extinction coefficient decreases as a function of T_A and Al% reaches low values in the visible and near-infrared ranges, as seen in figure 11 and figure 12. Which explains the transparent property of ZnO: Al% prepared films which suggested an optical windows application. Moreover, a slight increase of the k value can be explained by the metallic character of such oxide film [43]. Determination of the refractive index of thin films is important for optical applications. In optics, the refractive index "n" of an optical way is a dimensionless number that describes how light, or any other radiation, propagates through that medium. Refractive index is resolved from the absolute estimations of the absorbance and transmittance of the researched films utilizing the expression [44]:

$$n = \frac{1+R}{1-R} + \sqrt{\frac{4R}{(1-R)^2} - k^2} \quad \textbf{(12)}$$

Figure 12: Extinction coefficient k versus λ of ZnO:Al% thin films deposited at 370°C.

Where R is the optical reflectance. Plots in figure 13. represent the dispersion in the refractive index for the doped ZnO films in the investigated range of wavelengths, it indicates for all compositions that then decreases with increasing wavelength for all samples in the visible range. The calculated variation of n changeable with the wavelength for ZnO: Al% annealed at 370°C is shown in figure 14. We note that the n (ZnO: Al 0.6% and 5%) increase as a function of T_A, this is not the case for ZnO: Al 0.2%. the n (ZnO: Al 0.6% and 5%) behavior could be explained by the fact that the refractive index increased, which means the compactness of the film raise. For ZnO: Al 0.2% thin films are not the same case, this could be related to the type of the site occupation by Al.

(a)

(b)

(c)

Figure 13: Refractive index n(λ) of ZnO:Al 0.2% (a), ZnO:Al 0.6% (b) and ZnO:Al 5% (c) thin films deposited at various T_A.

Figure 14: Refractive index n(λ) of ZnO: Al% thin films deposited at 370°C.

In the same context, the variation of the porosity of our films is opposite to the behavior of the refractive index. Moreover, the exact origin of this behavior is the variation in defects such as V_O, O_i, zinc vacancies, Zun_i, and oxide antisites. The oxide antisites are the main cause of the opposite behavior in ZnO: Al 0.2% thin films. The slight increase in the values of k at the wide wavelengths is due to the contribution of the absorption of the free carriers which is much stronger in the doped layers. In addition, k (λ) decreases with the increase of T_A. The small values of k (λ) in [350-800] nm range, implies that these layers are transparent as shown in the transmission spectra. Furthermore, Akkari., *et al*. [45] suggested that the very low values of k indicate the surface smoothness and homogeneity of the films.

Dielectric characterization

From the refractive index and the extinction coefficient results, we have analyzed the real and imaginary parts of complex dielectric constant ε(λ) of ZnO: Al% (0.2%, 0.6%, and 5%) with annealing at different temperatures utilizing the next expression:

$$\varepsilon(\lambda) = \left(n(\lambda) - ik(\lambda)\right)^2 = \varepsilon_1(\lambda) - i\varepsilon_2(\lambda) \quad \textbf{(13)}$$

ε_1 and ε_2 are the real part of the permittivity and the imaginary part of the permittivity, respectively. figure 15 and figure 16 show the dielectric constants ε_1 and ε_2 in terms of wavelength. The estimations of ε_1 and ε_2 are concluded from n and k as indicated by surely understood relations [46]:

$$\varepsilon_1(\lambda) = n(\lambda)^2 - k(\lambda)^2 \quad \varepsilon_2(\lambda) = 2n(\lambda)k(\lambda)$$

(a)

(b)

(c)

Figure 15: Real part ε1 of the dielectric permittivity versus λ for different TA of ZnO:Al 0.2% (a), ZnO:Al 0.6% (b) and ZnO:Al 5% (c) thin films.

Figure 16: Real part ε1 of the dielectric permittivity versus λ for T = 370°C of ZnO: Al% thin films.

The dependence of the ε_1 on the wavelength is shown in figure 15 for the doped ZnO sample. Observe from this figure that the ε_1 depends on the refractive index by equation (14) because the effect of the extinction coefficient is very small maybe canceling. The ε_1 is increasing after annealing for all samples with increasing wavelength and with Al%, moving the vertex of the curve to higher wavelengths were happened with increasing Al% may be attributed to related ε_1 with refractive index by equation (14). The plots of ε_1 are similar to the refractive index because of the smaller values of k. The values of ε_2 depend mainly on the k values. ε_2 is lower than ε_1 which proves that the energy loss of light through thin films is low. Figure 15 and figure 16 reflect the same conclusion from the refractive index behavior. The ε_2 as a function of wavelength is shown in figure 17. The imaginary part depends on k by (15) because the n is very small [45]. Figure 17 and figure 18 show the presence of oscillations that decrease with increasing T_A. This leads to the decrease of the energy loss with T_A which is confirmed by the improvement of the crystalline quality of ZnO: Al% thin films with the increasing of T_A. This is consistent with the increase of the transmittance of films with increasing T_A. The ε_2 decrease as a function of T_A and Al% [48].

Cauchy model

The evolution of the refractive index concerning the Cauchy appropriation was watched in all ZnO: Al% thin films:

$$n = A + \frac{B}{\lambda^2} \qquad \textbf{(16)}$$

(a)

(b)

(c)

Figure 17: Imaginary part ε_2 of the dielectric permittivity versus λ of ZnO:Al 0.2% (a), ZnO:Al 0.6% (b) and ZnO:Al 5% (c) thin films deposited at various T_A.

Figure 18: Imaginary part ε_2 of the dielectric permittivity versus λ of ZnO: Al% thin films deposited at 370°C.

Where A, B, λ are the Cauchy's parameters and the wavelength of the used light, respectively, implying that the films have normal dispersion for the entire range of studied wavelengths.

Figure 19 depicts the evolution of refractive index n as a function of a square inverse wavelength and their fit by Cauchy law for ZnO: Al 0.2% at different T_A. Table 6 shows the Cauchy parameters and the static dielectric constant ε_s evolution for all samples. The Cauchy parameters and the static dielectric constant ε_s evolution as a function of Al%. We note that A decreases slightly with T_A increase, and its value is of the order of the ZnO thin film refractive index, whereas B increases as a function of Al% and decreases as a function of T_A for each Al%. The porosity is proportional to parameter B, which explain that the porosity increase as a function of Al%. The XRD parameters evolution such as microstrain and dislocation density reflects the impact of change in porosity and densification layers caused by relaxation and reorganization phenomena, which the evolution of the second Cauchy parameter reflects as a function of T_A and Al%. The estimations of Cauchy parameters have a huge relationship with the crystalline structure and the ionicity of ionic or covalent oxide materials.

	Film	A	B (nm^{-2})	ε_s
ZnO:Al 0.2%	RT	1.81	130513.19	3.28
	T_A = 220°C	1.75	111944.67	3.08
	T_A = 295°C	1.73	102229.28	3.02
	T_A = 370°C	1.67	97985.94	2.80
ZnO:Al 0.6%	RT	1.64	225149.32	2.7
	T_A = 220°C	1.60	160895.74	2.56
	T_A = 295°C	1.54	63963.50	2.38
	T_A = 370°C	1.70	107315.36	2.92
ZnO:Al 5%	RT	1.71	229216.27	2.95
	T_A = 220°C	1.67	109080.69	2.82
	T_A = 295°C	1.62	92385.84	2.65
	T_A = 370°C	1.58	84722.37	2.52

Table 6: Values of the fitting parameters A and B obtained by using the Cauchy law for ZnO: Al% thin films annealed at various temperatures.

Figure 19: Variation in the refractive index n as a function of $1/\lambda^2$ for ZnO: Al 0.2% thin films annealed at various temperature layers as deduced from Cauchy law fit.

Drude-Lorentz model

For larger wavelengths, Drude-Lorentz expression can explain the evolution of the real dielectric constant part ε_1 :

$$\varepsilon_1 = \varepsilon_\infty - \frac{\varepsilon_\infty \omega_p^2}{\omega^2} = \varepsilon_\infty - \frac{\varepsilon_\infty \omega_p^2}{4\pi^2 c^2}\lambda^2 = \varepsilon_\infty\left(1 - a\lambda^2\right) \quad (17)$$

Where ε_∞ and ω_p^2 are the limiting value of the high-frequency dielectric constant and the plasma frequency, respectively. $\omega_p^2 = Ne^2/\varepsilon_0 m_e^*$ with e, ε_0 and N/m_e^* are the elementary charge, the vacuum permittivity, and the ratio of carrier density to the effective mass. Figure 20 depicts the evolution of the real dielectric constant part ε_1 as a function of square wavelength for ZnO: Al 0.2% and shows the fits deduced by the Drude Lorentz model.

Figure 20: Variation in the real dielectric $_1$ constant part as a function λ^2 of for ZnO: Al 0.2% thin films annealed at various temperatures.

Table 7 shows the Drude Lorentz parameters for all samples. The Drude Lorentz parameters evolution as a function of Al%. This allows us to determine the evolution of ε_∞ and which respectively represent high-frequency dielectric constant and plasma frequency. We can conclude that the high-frequency dielectric constant ε_∞ decreases as a function of T_A this could be attributed to the structural defect variation as a function of temperature. Especially, the XRD results show that the crystallinity quality change as a function of T_A. On the other hand, the plasma frequency decrease as a function of T_A for both ZnO: Al 0.2% and 0.6%. In contrast, ZnO: Al 5% show inverse behavior this could be explained by the fact that Al species grow on the top of the ZnO network and they will change the conductor behavior. It is important to note that ZnO: Al 0.6% shows the high carrier density value this could be lead to say that the Al species don't grow on the top of the ZnO network but it is only growing into the ZnO network (V_0, Zun_i). These conclusions are in good agreement with the XRD data.

Film	ε_∞	ω_p^2 x10^{11} (rad^2 s^{-2})	N/m_e^* x10^{38} (m^{-3}kg^{-1})	Film
ZnO:Al 0.2%	RT	3.32	16.42	5.66
	T_A = 220°C	3.10	12.25	4.22
	T_A = 295°C	3.06	10.79	3.73
	T_A = 370°C	2.79	10.02	3.46
ZnO:Al 0.6%	RT	2.54	23.56	8.13
	T_A = 220°C	2.43	17.58	6.07
	T_A = 295°C	2.48	7.48	2.58
	T_A = 370°C	2.81	11.43	3.95
ZnO:Al 5%	RT	2.88	8.91	3.08
	T_A = 220°C	2.79	8.50	2.93
	T_A = 295°C	2.73	22.68	7.82
	T_A = 370°C	2.66	10.89	3.76

Table 7: Values of the high-frequency dielectric constant ε_∞, the plasma frequency ω_p^2, and the ratio of carrier density to the effective mass N/m_e^* of ZnO: Al% thin films annealed at various temperatures.

In conclusion, the values of ε_∞ are of the same order as those of the static dielectric constant are determined from the Cauchy model. The slight change in the carrier density to effective mass ratio may be caused by the change in the dipole-dipole interaction and relaxation phenomena, after the reorganization of the ZnO network as a function of T_A and Al%, between the ZnO network and Al species. This change could be explained by the probability of the reaction of other defects in the ZnO network. The analysis of the reflectance and transmittance spectra using a theoretical model allowed the determination of the optical parameters. The dependence of these parameters on the incident wavelength for the different samples has been analyzed using classical Cauchy, Drude–Lorentz, Tauc, and Urbach energy models and allowed the determination of pertinent optoelectronic parameters. The evolution of these optoelectronic parameters with T_A and Al% can be understood in terms of disorder caused by ZnO: Al% layers morphology change which is due to several transfer processes providing a variation in energy and relaxation in these thin films. The increase in Al species concentration leads to a decrease in ε_s, indicating a decrease in the densification of the material and a decrease in the energy gap improving the semiconductor character.

The evolution of optical parameters could be attributed to the imperfection in ZnO crystal, particle shape, and particle size. Since the doping did not affect the grain size significantly and the rod structure shape, the slight decrease or increase of E_g value might be due to the increase in the concentration of defects in the crystals with doping. The doping results in the rise of additional band

tail states, leading to shrinkage of the bandgap. This phenomenon, which causes the decrease in E_g, is generally in competition with another called: the Burstein Moss shift. This phenomenon induces an increase in the bandgap with the doping concentration [49]. The gap energy decrease or increases as a function of T_A or Al%, respectively. This evolution depicts the fact that our ZnO: Al% thin films based on ZnO: Al% powders fabricated via polyol show a competition between two phenomena, the first decrease the gap energy, and the second increase the gap energy. Each Al% and T_A combinations lead to a pertinent disorder and inhomogeneity of the layers.

Conclusion

ZnO: Al% thin films were prepared by spin-coating deposition method at atmospheric pressure followed by annealing. The effects of annealing and Al% on the structural and optical properties of the films were investigated. The XRD results show the presence of the rhombohedral polytypes occurring quite frequently in coexistence with their respective basic hexagonal. The XRD parameters evolutions strongly depend on T_A and Al%. Reflectance and transmittance analysis reflect the porosity, rugosity, relaxation, and reorganization of ZnO: Al% layers as a function of T_A and Al%. The dispersion of the films was studied using both the Cauchy model and the Drude-Lorentz method. Thin films of ZnO: Al% can be very promising and are subsequently a great potential in the field of the transparent cathode of organic optoelectronic devices, especially low T_A don't destroy the polymer chain in the active layers. Adsorption and desorption of oxygen are the main reasons which are controlling the conductivity of ZnO: Al% films.

Indeed, with a higher amount of defects, the electronic transition is made from the filled valence band to energy levels of defects. The doping results in the rise of additional band tail states. This is the first phenomenon that governs our layers. The presence of Burstein Moss shift in our layers as a function of Al doping concentration. This is the second phenomenon that tries to govern our layers. The Urbach and gap energy variation depict that disorder and inhomogeneity behavior phenomena control our layers and it is caused by competition between two of these possible phenomena. Under visible light irradiation by the introduction of the Al into the ZnO nanoparticles is not due only to the reduction of the gap value, but to the stimulation of electron exchanges with Al%. These phenomena open the opportunity to use our nanoparticles in other applications than solar cells such as photocatalysis.

Acknowledgement

The author extends her appreciation to the deputyship for Research and Innovation ministry of education in Saudi Arabia for funding this research work through the project number: rup-3.

Bibliography

1. J Dong., *et al*. "Effect of Al doping on performance of ZnO thin-film transistors". *Applied Surface Science* 433 (2018): 836-839.
2. O Kluth., *et al.* "Modified Thornton model for magnetron sputtered zinc oxide: film structure and etching behavior". *Thin Solid Films* 442 (2003): 80-85.
3. Alberti G., *et al*. "Efficiency Enhancement in ZnO: Al-Based Dye-Sensitized Solar Cells Structured with Sputtered TiO2 Blocking Layers". *The Journal of Physical Chemistry C*118 (2014): 6576-6585.
4. ST Shishiyanu., *et al*. "Sensing characteristics of tin-doped ZnO thin films as NO2 gas sensor". *Sensors and Actuators* B 107 (2005): 379-386.
5. NW Emanetoglu., *et al*. "Epitaxial ZnO piezoelectric thin films for saw filters". *Materials Science in Semiconductor Processing* 2 (1999): 247-252.
6. N Saito., *et al*. "Low-Temperature Fabrication of Light-Emitting Zinc Oxide Micropatterns Using Self-Assembled Monolayers". *Advanced Materials* 14 (2002): 418-421.
7. MH Huang., *et al*. "Room-temperature ultraviolet nanowire nanolasers". *Science* 292 (2001): 1897-9.
8. T David., *et al*. "Electro-optical and structural properties of thin ZnO films, prepared by filtered vacuum arc deposition". *Thin Solid Films* 447-448 (2004): 61-67.
9. BY Oh., *et al*. "Transparent conductive Al-doped ZnO films for liquid crystal displays". *Journal of Applied Physics* 99 (2006): 124505-124509.
10. K Mahmood and SB Park. "Atmospheric pressure based electrostatic spray deposition of transparent conductive ZnO and Al-doped ZnO (AZO) thin films: Effects of Al doping and annealing treatment". *Electronic Materials Letters* 9 (2013): 161-170.
11. WH Kim., *et al*. "Low-Pressure Chemical Vapor Deposition of Aluminum-Doped Zinc Oxide for Transparent Conducting Electrodes". *Journal of The Electrochemical Society* 158 (2011): 495-499.

12. AC Gâlcă., *et al*. "Optical properties of zinc oxide thin films doped with aluminum and lithium". *Thin Solid Films* 518 (2010): 4603-4606.

13. V Shelke., *et al*. "Effect of open air annealing on spin coated aluminum doped ZnO nanostructure". Materials Chemistry, and Physics 141 (2013): 81-88.

14. B Arif. "Determination of optical constants of ZnO growth by PECVD Method". *Journal of Materials and Electronic Devices* 1 (2015): 28-32.

15. Mezni F., *et al*. "Facile synthesis of ZnO nanocrystals in polyol". *Materials Letterst* 86 (2012): 153-156.

16. M Louhichi., *et al*. "Structural and photoluminescence properties of Al-doped zinc oxide nanoparticles synthesized in polyol". *Applied Surface Science* 356 (2015): 998-1004.

17. BJ Jin., *et al*. "*Thin Solid Films* 366 (2000): 107-110.

18. YP Rakovich., *et al*. "*Physica Status Solidi A* 206 (2009): 2497-2509.

19. J Gosh., *et al*. "Tuning the visible photoluminescence in Al doped ZnO thin film and its application in label-free glucose detection". *Sensors, and Actuators, B: Chemical* 254 (2018): 681-689.

20. LC Damonte., *et al*. "Structural and electronic properties of Al-doped ZnO semiconductor nanopowders: Interplay between XRD and PALS experiments and first-principles/DFT modeling". *Journal of Alloys and Compounds* 735 (2018): 2471-2478.

21. JI Hanoka and V Vand. "Further Studies of Polytypism in Lead Iodide". *Journal of Applied Physics* 39 (1968): 5288-5297.

22. G Lal and GC Trigunayat "Phase transformations at high temperatures in polytypic crystals of cadmium iodide". *Journal of Crystal Growth* 11 (1971): 177-181.

23. MM Uplane., *et al*. "Structural, optical and electrochromic properties of nickel oxide thin films grown from electrodeposited nickel sulfide". *Applied Surface Science* 253 (2007): 9365-9371.

24. R Tripathi., *et al*. "Dielectric relaxation of ZnO nanostructure synthesized by soft chemical method". *Current Applied Physics* 10 (2010): 676-681.

25. Boukhachem B., *et al*. "Structural, opto-thermal and electrical properties of ZnO: Mo sprayed thin films". *Materials Science in Semiconductor Processing* 15 (2012): 282-292.

26. XS Wang., *et al*. "Ferroelectric and dielectric properties of Li-doped ZnO thin films prepared by pulsed laser deposition". *Applied Physics A* 77 (2003): 561-565.

27. MA Mahdi., *et al*. "Structural and optical properties of nanocrystalline CdS thin films prepared using microwave-assisted chemical bath deposition". *Thin Solid Films* 520 (2012): 3477-3484.

28. GH Jo. "Enhanced electrical and optical properties based on stress reduced graded structure of Al-doped ZnO thin films". *Ceramics International* 44 (2018): 735-741.

29. H Li., *et al*. "Optical and structural analysis of rare earth and Li co-doped ZnO nanoparticles". *Journal of Alloys and Compounds* 550 (2013): 526-530.

30. M Shaban and AM ElSayed. "Effects of lanthanum and sodium on the structural, optical and hydrophilic properties of sol-gel derived ZnO films: A comparative study". *Materials Science in Semiconductor Processing* 41 (2016): 323-334.

31. T Saidani., *et al*. "Influence of annealing temperature on the structural, morphological and optical properties of Cu doped ZnO thin films deposited by the sol-gel method". *Superlattices, and Microstructures* 75 (2014): 47-53.

32. M Li., *et al*. "A comparative study of growth and properties of atomic layer deposited transparent conductive oxide of Al-doped ZnO films from different Al precursors". *Thin Solid Films* 646 (2018): 126-131.

33. HJ Al-Asedy., *et al*. "Structure, morphology and photoluminescence attributes of Al/Ga co-doped ZnO nanofilms: Role of annealing time". *Materials Research Bulletin* 97 (2018): 71-80.

34. KM Sandeep., *et al*. "Nonlinear absorption properties of ZnO and Al-doped ZnO thin films under continuous and pulsed modes of operations". *Optics and Laser Technology* 102 (2018): 147-152.

35. S Belgacem and R Bennaceur. "Propriétés optiques des couches minces de SnO2 et CuInS2 airless spray". *Review of Physics Applied* 25 (1990): 1245-1258.

36. M Caglar M., *et al*. "Influence of dopant concentration on the optical properties of ZnO: In films by sol-gel method". *Thin Solid Films* 517 (2009): 5023-5028.

37. AF Akta Ruzzuman., *et al*. "Electrical, optical and annealing characteristics of ZnO: Al films prepared by spray pyrolysis". *Thin Solid Films* 198 (1991): 67-74.

38. CM Muiva., *et al*. "Effect of doping concentration on the properties of aluminum-doped zinc oxide thin films prepared by spray pyrolysis for transparent electrode applications". *Ceramics International* 37 (2011): 555-560.

39. J Lv., *et al*. "Effect of annealing temperature on photocatalytic activity of ZnO thin films prepared by sol-gel method". *Superlattices, and Microstructures* 50 (2011): 98-106.

40. M Caglar., *et al*. "Temperature dependence of the optical band gap and electrical conductivity of sol-gel derived undoped and Li-doped ZnO films". *Applied Surface Science* 256 (2010): 4966-4971.

41. J Ungula., *et al*. "Bandgap engineering, enhanced morphology and photoluminescence of un-doped, Ga and/or Al-doped ZnO nanoparticles by reflux precipitation method". *Journal of Luminescence* 195 (2018): 54-60.

42. VK Miloslavskii and PS Pogrebniak. "The Burstein-Moss Effect in Polycrystalline ZnO Films". *Physics State Solid* (b) 51 (1972): 99-102.

43. R Mimouni., *et al*. "Investigation of structural and optical properties in Cobalt-Chromium co-doped ZnO thin films within the Lattice Compatibility Theory scope". *Journal of Alloys and Compounds* 624 (2015): 189-194.

44. C Mrabet., *et al*. "Some physical investigations on hexagonal-shaped nanorods of lanthanum-doped ZnO". *Journal of Alloys and Compound*s 648 (2015): 826-837.

45. W Al-Taa'y., *et al*. "Effect of Nano ZnO on the Optical Properties of Poly (vinyl chloride): Films". *International Journal of Polymer Science* 2014 (2014): 1-6.

46. Akkari C., *et al*. "Optical study of zinc blend SnS and cubic In2S3:Al thin films prepared by chemical bath deposition". *Journal of Material Science* 46 (2011): 6285-6292.

47. M Sesha Reddy., *et al*. "Optical constants of polycrystalline CuGaTe2 films". *Optical Materials* 4 (1995): 787-790.

48. A Boukhachem., *et al*. "Physical investigations on MoO3 sprayed thin film for selective sensitivity applications". *Ceramics International* 40 (2014): 13427-13435.

49. AK Walton and TS Moss. "Determination of Refractive Index and Correction to Effective Electron Mass in PbTe and PbSe". *Proceedings of the Physical Society* 81 (1963): 509-513.

50. W Zhang. "Tailoring of optical and electrical properties of transparent and conductive Al-doped ZnO films by adjustment of Al concentration". *Materials Science in Semiconductor Processing* 74 (2018): :147-153.

51. R Boughalmi., *et al*. "Effect of tin content on the electrical and optical properties of sprayed silver sulfide semiconductor thin films". *Material Science Semiconductor Processing* 16 (2013): 1584-1591.